# Shear-driven vertical mixing and turbulent exchange over the continental slope in the northwestern Sea of Japan

Dmitry Stepanov[1*], Alexander Ostrovskii[2†], Evgeny Ryzhov[1†], Alexander Lazaryuk[1†]

[1*]V.I.Il'ichev Pacific Oceanological Institute of Far Eastern Branch Russian Academy of Sciences, 43 Baltiyskaya, Vladivostok, 690041, Russia.
[2]Shirshov Institute of Oceanology, Russian Academy of Sciences, 36 Nahimovskiy prospekt, Moscow, 117997, Russia.

*Corresponding author(s). E-mail(s): step-nov@poi.dvo.ru;
Contributing authors: osasha@ocean.ru; ryzhovea@poi.dvo.ru;
lazaryuk@poi.dvo.ru;
[†]These authors contributed equally to this work.

**Abstract**

Using fine-scale measurements in the northwestern Sea of Japan, we estimated the vertical mixing parameters in the sea water column extended from the lower part of the thermocline downward to the near-bottom layer above the continental slope. The vertical scales of the turbulent patches were determined together with the turbulent dissipation rate and diapycnal diffusivity based on the conductivity, temperature, and depth data obtained by an Aqualog moored profiler from April through October 2015. The Thorpe-scale method was used to estimate the vertical mixing parameters as well as the vertical heat and salt fluxes. The enhanced vertical mixing, as well as enhanced upward heat flux and downward salt flux, occurred below the mixed layer despite strong density stratification. By comparing the turbulent dissipation rate and diapycnal diffusivity estimates derived via the Thorpe-scale method and the estimates of the same parameters obtained earlier by applying the finescale parameterization method to the same dataset in addition to the collocates of the current velocity measurements, the comparative accuracy evaluation of both methods was carried out. Finally, by compiling the vertical mixing data obtained by the Thorpe-scale method and the finescale parameterization approach, the generalized depth profile for the background diapycnal diffusivity is presented for the depth range from 70 to 350 m.

**Keywords:** vertical mixing, the Sea of Japan, Thorpe-scale method, finescale parameterization

# 1 Introduction

Located at the northwestern margin of the Pacific, the deep semi-enclosed Sea of Japan (hereinafter referred to as the Sea) is renowned to the world oceanographers as a basin that provides opportunities for researchers to conduct large-scale oceanographic experiments (Gamo et al, 2014). The Sea dynamics feature processes typical of the ocean (Chang et al, 2015). Among these, one of the most interesting is the strong ventilation of the Sea intermediate and deep layers. In the winter, during intensive northeasterly monsoon cooling, deep convection develops in the northwestern part of the Sea. Cold and fresh water as well as chemical tracers penetrate more than 1000 m below the surface (Talley et al, 2003, 2006). It is believed that deep convection began to slow in the 1960s or earlier (Kim et al, 2001, 2002), yet the intermediate and deep layers of the Sea remain well mixed. This implies that turbulent mixing could have become relatively more important in the past several decades in the Sea.

In the deep ocean, vertical mixing is generally caused by wind forcing and breaking of internal gravity waves, which are generated by the tide-topography interactions (Wunsch and Ferrari, 2004; Waterhouse et al, 2014; MacKinnon et al, 2017; Gregg et al, 2018). In particular, internal lee waves can be driven by the interaction of shear currents with the topography (MacKinnon et al, 2017; Nikurashin et al, 2014). Notably, the semidiurnal tide enters the Sea through the wide Tsushima Strait in the southern region and then propagates toward the northern continental slope. Although the tide wave weakens when it passes northward through the Sea, its energy is still high when it arrives at the continental slope and shelf (Jeon et al, 2014), where it induces internal gravity waves. Ostrovskii et al (2021) assessed the turbulent mixing that can be generated by the shear-driven instabilities associated with breaking internal gravity waves over the Sea continental slope. The finescale parametrization framework (FSP) (Henyey et al, 1986; Polzin et al, 1995, 2014; Kunze et al, 2002; MacKinnon et al, 2013; Meyer et al, 2015; Hibiya et al, 2012; Gregg et al, 2018) that assumes that internal gravity wave breaking makes a major contribution to vertical mixing was applied to the *in situ* data for the thermohaline structure and the current shear to assess the turbulent dissipation rate and diapycnal diffusivity. The fine-structure vertical resolution collocated data were measured using an Aqualog profiler southeast of Peter the Great Bay of the Sea in April-October 2015 (Lazaryuk et al, 2017).

The estimates of diapycnal diffusivity indicated that the vertical exchange of heat, salt and dissolved oxygen was enhanced under the seasonal pycnocline in the warm half-year. The FSP framework requires knowledge of the low-wavenumber shear and strain variances (Polzin et al, 2014; Kunze et al, 2006; Lique et al, 2014). To comply with this condition, the spectra of the shear and strain had to be estimated using vertical segments spanning more than or equal to 128 dbar. Because the data for the sea near-surface layer were unavailable, the layer below the mixed layer (Lim et al, 2012) was not considered in the paper by Ostrovskii et al (2021). Mesoscale eddies can also affect vertical mixing (Whalen et al, 2015; Kunze et al, 1995; You et al, 2021; Yang et al, 2017). Anticyclonic mesoscale eddies are well-developed in the northern Japan basin, and the data show that turbulent mixing is stronger at the edges and bottom parts of eddies (Ostrovskii et al, 2021, 2023).

In addition to the abovementioned processes, vertical mixing can be driven by double diffusion (Lee et al, 2014; Inoue et al, 2007; Radko and Smith, 2012). Double diffusion signatures were also found in the Sea (Stepanov et al, 2023). Using the abovementioned Aqualog

profiler dataset, Stepanov et al (2023) studied fine-scale mixing associated with double diffusion processes: salt fingers and thermal convection. Based on the Turner angle analysis and estimates of the effective diffusivities of heat and salt (Inoue et al, 2007) derived from moored profiler Aqualog data, it was found that in the spring, thermal convection dominated the vertical mixing in the upper layer of the Sea between 70 m and 200 m. Double diffusion processes occurred sporadically in the upper layer, while shear-driven instabilities played the leading role in vertical mixing generation.

In this study, we focused on the estimation of the vertical mixing and turbulent exchange in the upper part of the Sea immediately below the near-surface layer through a further analysis of the moored profiler Aqualog dataset. The upper part of the Sea water column was not considered in a previous study (Ostrovskii et al, 2021) due to the limitations of the FSP framework. In the following, we apply the Thorpe-scale method (TSM) (Thorpe, 1977; Smith, 2020; MacKinnon et al, 2017; Thompson et al, 2007) to the depth profiles of the water density to estimate the turbulent patch vertical scale by applying a special reordering of the data, as described below. The derived estimates are used to assess the turbulent dissipation rate. This approach requires high-resolution depth profiles of temperature and salinity with the background of a large vertical density gradient (Dillon, 1982; Stansfield et al, 2001; Thompson et al, 2007). The TSM allows us to quantify the manifestations of turbulence regardless of its cause, assuming that these manifestations are associated with density overturns in the turbulent area. For clarity, to focus on turbulent mixing only, the time periods in which thermal convection and salt fingers prevailed in vertical mixing (Stepanov et al, 2023) must be excluded from this analysis. The estimates of the vertical mixing parameters derived using the TSM are compared with those obtained within the FSP framework. Therefore, we aim to obtain a more comprehensive overview of the vertical mixing in the intermediate waters in the northwestern Sea during the warm half-year.

The rest of the paper is organized as follows. The dataset used is presented in Sect. 2. The Thorpe-scale method and the FSP framework are described in Sect. 3. The conditions for the shear-driven turbulence, estimates of the turbulent dissipation rate and diapycnal diffusivity as well as the vertical heat and salt fluxes and their depth and temporal variations during the survey are presented in Sect. 4. The discussion in Sect. 5 is based on a comparison of the vertical mixing estimates derived from the TSM and the FSP framework. Additionally, the vertical distribution of the mixing processes is presented. Sect. 6 summarizes our findings.

## 2 Dataset

To quantify vertical mixing, we analyzed fine-structure measurements of temperature ($T$) and salinity ($S$) collected by an Aqualog profiler during a survey from mid-April to mid-October 2015. The Aqualog profiler was moored on the continental slope in the northwestern Sea (Fig. 1). The depth of the mooring station was approximately 425 m. The profiler crawled up and down a taut mooring wire at a vertical speed of 0.2 m $s^{-1}$. During the first five days, the Aqualog profiler moved from 70 to 260 m, and on the sixth day, the profiler moved further downward to 420 m to obtain full-depth profiles. This regular operation pattern was repeated until mid-October. In total, 1550 sets of vertical profiles of the measured parameters were obtained. The profiler was equipped with a Sea-Bird-Electronics (SBE) CTD 52-MP, maintaining a sampling rate of 1 Hz, and a Nortek Aquadop, with a sampling rate of 23 Hz. A

detailed description of the survey measurements was provided by Ostrovskii et al (2021). During the survey, the Sea processes near the mooring station were affected by the Primorye Current and by wind forcing.

The depth profiles of the salinity were processed following to the method of (Lazaryuk et al, 2017). The potential density ($\sigma_\theta$) was calculated from the $T$ and $S$ data using the Thermodynamic Equation of SeaWater 2010 (TEOS-10) (McDougall and Barker, 2011). The depth profiles of the potential density were used to estimate the Thorpe scale ($L_T$), the turbulent dissipation rate ($\varepsilon_K$) and the diapycnal diffusivity ($K_\rho$).

# 3 Thorpe-Scale Method and the Finescale Parameterization Framework

We suggest that turbulence is sustained by a shear-driven mechanism and exclude other mechanisms, e.g., double diffusive and convection cases, from consideration. To quantitatively assess vertical mixing, we apply the conventional parameterization (Osborn, 1980):

$$K_\rho = \Gamma \varepsilon_K / N^2, \tag{1}$$

where $\Gamma$ is the mixing efficiency and $N$ is the buoyancy frequency. Mashayek et al (2017) noted that $\Gamma$ varies significantly due to the modulation of vertical mixing by dynamic processes. $\Gamma$ is typically equal to 0.2. Note that $N$ represents the background stratification. $N$ is estimated over a 36-dbar depth span, and a 14-day window is subsequently used for the time averaging of $N^2$.

We assess $\varepsilon_K$ according to the method of Dougherty (1961) and Ozmidov (1965), assuming that there is a vertical scale ($L_O$) for which stratification inhibits the extent of the turbulent patch:

$$L_O = \left(\varepsilon_K / N^3\right)^{1/2}. \tag{2}$$

Thorpe (1977) suggested that scale (2) can be estimated by reordering a depth profile of density $\sigma_\theta$, which contains a turbulent patch, to the steady density profile as follows:

$$L_T = \langle (z_n - z_m)^2 \rangle_z^{1/2}, \;\; n \in R \tag{3}$$

where $\langle ... \rangle_z$ denotes the average over the turbulent patch and $R$ is the set of the fluid elements within the turbulent patch. These fluid elements are located at depths $z_n$ and after reordering the density profile, the fluid elements are located at depths $z_m$ (for example, Fig. 2). Based on direct dissipation measurements in a sheared thermocline, Dillon (1982) proposed the relation between the $L_T$ and $L_O$, namely $L_0 \approx 0.8 L_T$. Using relation (2), $\varepsilon_K$ can be estimated as follows:

$$\varepsilon_K = L_O^2 N^3 \approx 0.64 L_T^2 N^3. \tag{4}$$

Note that in (2) and (4), $N$ is the stratification of the specific turbulent patch (Thompson et al, 2007).

In applying the TSM, we face an issue associated with "salinity spiking" when different ensembles of the $T$ and $S$ data may have the same density. To avoid uncertainty, the first 30 and last 180 data samples were excluded from each profile of $T$ and $S$.

Thorpe (1977) noted that this method cannot be applied in the regions dominated by thermal convection and double diffusion. Based on these results (Stepanov et al, 2023), events associated with double diffusion processes, i.e., diffusion convection and salt fingers, were omitted from further consideration. We also exclude the turbulent patches where the necessary condition for double diffusion is satisfied. The Turner angle (Ruddick, 1983; Stepanov et al, 2023) was estimated using the TEOS-10 algorithm (McDougall and Barker, 2011).

All of the profiles ($\varepsilon_K$ or $K_\rho$) are binned into 10-m layers. For all median values, the confidence intervals (95% level) were evaluated using the bootstrap technique (Efron and Gong, 1983) and the bootstrap toolbox (Zoubir and Boashash, 1998).

When diapycnal diffusivity (1) is known, the vertical heat and salt fluxes can be estimated as follows:

$$Q = -c_p \rho_0 K_\rho \frac{\partial \langle \theta \rangle_t}{\partial z}, \; J_S = -K_\rho \frac{\partial \langle S \rangle_t}{\partial z}, \tag{5}$$

where $\langle ... \rangle_t$ denotes the time average, $\theta$ is the potential temperature, $c_p$ is the specific heat of seawater which is equal to 4000 J kg$^{-1}$ K$^{-1}$ and $\rho_0$ is the seawater density of 1025 kg m$^{-3}$. Note that the $\theta$ and $S$ data are binned into 2-dbar layers. The vertical gradients of $\theta$ and $S$ are calculated over a 10-dbar scale and a 14-day window is subsequently used for the time averaging of the vertical gradients. $L_T$, $\varepsilon_K$ and $K_\rho$ are estimated for each profile of $\sigma_\theta$.

For a more detailed explanation of the TSM framework, let us consider an example of $\sigma_\theta$ and the profiles derived by applying the Thorpe scale analysis (Fig. 2). The profile of $\sigma_\theta$ was collected by a moving-down Aqualog profiler at 00 h 18 s on April 26, 2015. This profile features manifestations of shear-driven turbulence within the depth range from 70 to 160 m (Fig. 2a). For example, from 80 to 100 m, the value of $\sigma_\theta$ at the specified depth level is greater than that at the next depth level. The density stratification from 80 to 100 m is weak, and its value is $N = 1.2$ cph (Figure 2b). The Thorpe displacement $L_D = (z_n - z_m)$ (3) results in values ranging from -8 m to 8 m, such that $L_T = 4$ m and $\varepsilon_K$ reaches $10^{-10}$ W kg$^{-1}$.

For greater confidence in our estimates, we compare $\varepsilon_K$ and $K_\rho$ derived from the TSM with those from the FSP framework. The turbulent dissipation rate ($\varepsilon_K^{FSP}$) and diapycnal diffusivity ($K_\rho^{FSP}$) derived from the FSP framework were estimated as described previously (Ostrovskii et al, 2021). To obtain $\varepsilon_K^{FSP}$, we applied the following relation (Henyey et al, 1986; Gregg and Kunze, 1991; Polzin et al, 1995; Gregg et al, 2003; Fer et al, 2010; Meyer et al, 2015):

$$\varepsilon_K^{FSP} = \varepsilon_0 \frac{N^2}{N_0^2} \frac{\left(\widehat{S_z^2}\right)^2}{\left(\widehat{S_{zGM}^2}\right)^2} \frac{3\,(R_w + 1)}{2\sqrt{2} R_w \sqrt{R_w - 1}} \frac{f \cosh^{-1}(N/f)}{f_0 \cosh^{-1}(N_0/f_0)} \tag{6}$$

which depends on the integrated variance in the observed vertical shear ($\widehat{S_z^2}$) and the shear-to-strain ratio ($R_w$) (Ostrovskii et al, 2021). In (6) the constants are defined according to the modified Garrett-Munk model (Garrett and Munk, 1972; Cairns and Williams, 1976) for the

reference latitude 32.5°N: $\varepsilon_0 = 8.0 \cdot 10^{-10}$ W kg$^{-1}$, $N_0 = 3$ cph, and $f_0 = 7.8 \cdot 10^{-5}$ rad s$^{-1}$. At the observational site at 42.6° N in the northwestern Sea, the local inertial frequency was $f = 9.87 \cdot 10^{-5}$ rad s$^{-1}$. Note that relation (6) depends on the vertical shear, which was estimated from high-vertical-resolution measurements of the horizontal velocity components (see the above Sec. 2). Using relation (6), $\varepsilon_K^{FSP}$ is estimated for the layers with weak density stratification, where the strain estimates are less reliable. Then, to estimate $K_\rho^{FSP}$, the Osborn relation (1) was applied. The $\varepsilon_K^{FSP}$ and $K_\rho^{FSP}$ profiles were binned into a 10-m thick layer.

# 4 Results

## 4.1 Necessary conditions for shear-driven turbulence

When analyzing the vertical mixing associated with shear-driven turbulence, the necessary conditions for its generation should be considered. Density stratification is a leading factor influencing the shear-driven turbulence evolution. A high density stratification unfavorably affects the development of shear-driven turbulence. By contrast, the extent (spatial scale) of the turbulence motion is large for weak density stratification. The values of $N$ reach high values of more than 3 cph in the upper layer at the depth from 65 to 150 m (Fig. 3). From mid-April to the end of May, maximum $N$ values ranging from 2.5 to 3 cph are found below the mixed layer and down to the depth of 100 m. From June to October, the maximum values of $N$ occur at the depths ranging from 65 to 180 m. At the depths greater than 200 m, density stratification weakens, and the value of $N$ decreases from 2.6 to 1.5 cph. It appears that strong density stratification events during the survey suppress the development of shear-driven turbulence.

We estimate the gradient Richardson number ($Ri$), as a principal measure of instability, according to (Miles, 1961) as follows:

$$Ri = \frac{\langle N^2 \rangle_t}{V_z^2} < 0.25, \tag{7}$$

where $V_z^2 = \left( \left[ \frac{\partial u}{\partial z} \right]^2 + \left[ \frac{\partial v}{\partial z} \right]^2 \right)$ is the vertical shear of the horizontal velocity component $(u, v)$.

For $Ri < 0.25$, we expect that the necessary condition for the development of shear-driven turbulence is satisfied. Figure 4 shows the evolution of $Ri$ during the survey. Notice that the regions of the data profiles where double diffusion was developed (Stepanov et al, 2023) are excluded from this analysis. From mid-April to mid-June 2015, despite strong stratification in the upper layer, $Ri < 0.25$ was often observed at the depths of 70–260 m. From mid-June 2015 to October, due to increasing density stratification in the upper layer, the necessary conditions were satisfied mainly in the Sea layer at the depths of more than 150 m. However, in some cases the condition $Ri < 0.25$ was fulfilled in the layer at the depths of 70–150 m. Later, in October, the condition $Ri < 0.25$ was fulfilled in the layer at the depths of 70-260 m. Thus, one can expect strong shear-driven turbulence manifestations in the form of turbulent patches with various length scales in the Sea upper layer despite the presence of strong density stratification in this layer.

## 4.2 Thorpe scale estimates of $\varepsilon_K$ and $K_\rho$

In this subsection, we focus on the estimates of $\varepsilon_K$ and $K_\rho$ obtained using the TSM and relation (1). We aim to obtain a set of estimates that match those derived earlier by using FSP frameworks; therefore, the same data profiles were taken for the analysis as in Ostrovskii et al (2021). Figure 5 shows the TSM estimates of $\varepsilon_K$. Note that the values of $\varepsilon_K < 10^{-20}$ W kg$^{-1}$ and $K_\rho < 10^{-7}$ m$^2$ s$^{-1}$ are not shown. Additionally, if any $\sigma_\theta$ profile did not have at least one density overturn, this profile was excluded from the analysis.

In the upper layer at the depths from 70 to 150 m, the values of $\varepsilon_K$ range from $10^{-9}$ to $10^{-7}$ W kg$^{-1}$, whereas in the lower layer at the depths from 150 to 200 m, they decrease by two orders of magnitude and become negligible at $10^{-11}$ W kg$^{-1}$. However, sometimes high values of $\varepsilon_K$ occur at the depths greater than 200 m; for example, on 23 September, $\varepsilon_K$ was equal to $10^{-6}$ W kg$^{-1}$. The time-depth distribution of the estimated values is rather sparse because we omit the data when other mixing processes, such as double diffusion, dominate (Stepanov et al, 2023). High $\varepsilon_K$ values in the upper layer at the depths from 70 to 180 m indicate greater dissipation of turbulent kinetic energy.

The high dissipation rate of turbulence results in large estimates of the diapycnal diffusivity $K_\rho$. In particular, $K_\rho$ is often as high as $10^{-4}$–$10^{-3}$ m$^2$ s$^{-1}$ in the upper layer at the depths from 70 to 180 m (Figure 5b). Occasionally large $K_\rho$ values in the deep layer are due to high turbulent dissipation and weak dependence on density stratification (Fig. 3).

The survey median values are more suitable for demonstrating typical vertical distributions of $\varepsilon_K$ and $K_\rho$ (Fig. 6). Higher survey median values from $10^{-8}$ to $\sim 10^{-10}$ W kg$^{-1}$ and from $\sim 10^{-4}$ to $10^{-5}$ m$^2$ s$^{-1}$ are found in the upper layer at the depths from 70 to 180 m. In the depth range from 190 to 300 m, the survey median values of $\varepsilon_K$ and $K_\rho$ decrease to $5 \cdot 10^{-11}$ W kg$^{-1}$ and $5 \cdot 10^{-6}$ m$^2$ s$^{-1}$, respectively, so that the uncertainty of both estimates is large, as indicated by the confidence intervals. At the depths of less than 370 m, the median survey values of $\varepsilon_K$ and $K_\rho$ tend to increase. The median survey values of $\varepsilon_K$ and $K_\rho$ increase to $\sim 10^{-10}$ W kg$^{-1}$ and $\sim 10^{-5}$ m$^2$ s$^{-1}$, respectively.

Let us demonstrate the survey-median profiles of $\varepsilon_K$ and $K_\rho$ for the layer at the depths 70–260 m computed from all of the data (Fig. 7), rather than only from the full-depth profiles, as shown in Fig. 6. The median survey values of $\varepsilon_K$ peak at $3 - 4 \cdot 10^{-9}$ W kg$^{-1}$ in the layer at the depths from 70 to 100 m, whereas in the layer below, down to a depth of 250 m, the median survey estimates of $\varepsilon_K$ decrease with depth to approximately $5 \cdot 10^{-11}$ W kg$^{-1}$. The survey-median $K_\rho$ profile is similar to the survey-median $\varepsilon_K$ profile. In the layer at the depths from 70 to 100 m, the survey-median $K_\rho$ values vary from 3 to $4 \cdot 10^{-5}$ m$^2$ s$^{-1}$, and the highest $K_\rho$ values reach approximately $3.5 \cdot 10^{-5}$ m$^2$ s$^{-1}$ at the depths of 100–120 m. Downward, the survey-median $K_\rho$ decreases toward $\sim 10^{-6}$ m$^2$ s$^{-1}$ at the depth of 250 m.

## 4.3 Vertical heat and salt fluxes

Estimates of diapycnal diffusivity allow us to assess the vertical fluxes of heat and salt (5). First, let us focus on the time-depth variations in $Q$ in the upper layer (Fig. 8a). The flux $Q$ is usually directed downward during the survey. A single period was found when a $Q$ of –6 W m$^{-2}$ was directed upward from mid-April to May. From May through August, the median value of $Q$ decreased from 2.2 W m$^{-2}$ at 70 m depth to 0.1 W m$^{-2}$ at 200 m depth. In the summer, about 20% values of $Q$ reached a positive value of more than 10 W m$^{-2}$ at the depths

from 70 to 150 m. In the autumn, higher values of the flux were observed down to the depth of 180 m. For depths greater than 200 m, the vertical heat flux decreased from June through October.

Figure 8b shows that $J_S$ was mainly negative during the survey, indicating that $J_S$ was basically directed upward. However, events associated with positive $J_S$ values were observed in the layer at the depths from 70 to 130 m, reaching $J_S$ of $3 \cdot 10^{-9}$ (kg salt) (kg seawater)$^{-1}$ m s$^{-1}$. High negative $J_S$ values of $-5 \cdot 10^{-9}$ (kg salt) (kg seawater)$^{-1}$ m s$^{-1}$ were observed from mid-April through May. Additionally, the strong weakening of the $J_S$ at the depths greater than 180 m occurred from June through October.

# 5 Discussion

The enhanced vertical mixing, revealed by using the TSM below the mixed layer, was associated with the basin-scale shear current. In the sea upper layer, the higher diapycnal diffusivity can be associated with the vertical shear induced by Ekman pumping. The effects of near-inertial internal waves induced by wind forcing also enhance the mixing. The shear instabilities associated with internal waves can be important for vertical mixing in the Sea. Near-inertial oscillations are observed over the northwestern sea shelf (Yaroshchuk et al, 2016). The dynamic conditions in the northwestern Sea featuring cyclonic gyre, coastal jet currents, and mesoscale and sub-mesoscale eddies are similar to those in certain marginal seas, such as the northwestern Mediterranean Sea and the northern Black Sea. Podymov et al (2020) quantified vertical mixing near the northeastern Black Sea continental slope using measurements of sea temperature, conductivity, and current velocity by a collocated moored Aqualog profiler during 2013–2016. The calculations were performed according to the well-known parametrization of the vertical turbulent exchange coefficient based on the Richardson number, originally proposed by Munk and Anderson (1948). The data analysis indicated that the diapycnal diffusivity was the highest at approximately $10^{-4} - 3 \cdot 10^{-4}$ m$^2$ s$^{-1}$ at the depths ranging from 50 to 100 m.

The Sea undergoes strong atmospheric forcing. The passage of atmospheric cycles leads to frequent adjustment of the geostrophic balance of the Sea and a release of the available potential energy. Eventually, this energy impact can result in vertical mixing in the Sea, including in the continental slope area. Notably, high turbulent dissipation rates ranging from $10^{-9}$ W kg$^{-1}$ to $10^{-8}$ W kg$^{-1}$ were observed below the mixed layer in the southeastern Sea, where the Tsushima Warm Current propagates Kawaguchi et al (2021). Kawaguchi et al (2021) noted that enhanced vertical mixing was modulated by mesoscale dynamics. Noticeably, the estimates obtained by Kawaguchi et al (2021) are close to our results obtained by applying the TSM for analysis of the moored Aqualog profiler data in the Primorye Current region of the northwestern Sea. In the regions where shear flow dominates and wind forcing exhibits strong spatio-temporal variability, enhancement of vertical mixing below the mixed layer can be expected.

The TSM approach has been used to study vertical mixing from CTD profiles for several regions of the world ocean. Similar to the observations in the upper layer, enhanced vertical mixing was found both in the winter and in the summer of 1998 in the upper layer at the depths from 70 to 120 m in the Juan de Fuca Strait, where the shear flow was strong (Stansfield et al, 2001). The Thorpe scale, turbulent dissipation rate and diapycnal diffusivity were estimated.

The estimates of diapycnal diffusivity in the Juan de Fuca Strait by Stansfield et al (2001) are of the same order of magnitude ($10^{-4}$ m$^2$ s$^{-1}$) as those in our study for the northwestern Sea.

The intense turbulence patches under the mixed layer and the high vertical gradients of temperature and salinity often lead to the spots with enhanced vertical heat and salt exchanges. The increased vertical heat exchange was as large as $10^4$ W m$^{-2}$ with a 3-day averaged flux of about 300 W m$^{-2}$ on the southwestern boundary of the Ulleung Basin in the Sea (Wijesekera et al, 2022), where vertical mixing was studied using combined ship-based, moored, and quasi-autonomous observations. Notice that Wijesekera et al (2022) highlighted the enhanced vertical mixing below the mixed layer.

## 5.1 Comparison of the TSM and FSP approaches for quantifying turbulent mixing

In Sect. 4 above, we used the TSM to quantify the vertical mixing in the layer at the depths from 70 to 150 m, which was not considered in previous work, partly due to limitations of the FSP framework (Ostrovskii et al, 2021). On the one hand, the TSM has known constraints. Due to weak density stratification, the turbulent dissipation rate can be underestimated. On the other hand, the FSP framework has its own limitations, which do not allow us to obtain the full-depth pattern of diapycnal diffusivity based on the FSP approach alone. The two methods can potentially complement each other if the TSM is applied to the upper portion of the sea water column and the FSP is used for the deeper layers. Furthermore, comparison of the results obtained by both methods will be useful for better understanding of their utility.

We compare the median survey values of $\varepsilon_K$ and $K_\rho$ estimated using the TSM (Fig. 6) and those derived by Ostrovskii et al (2021) using the FSP framework ($\varepsilon_K^{FSP}$ and $K_\rho^{FSP}$). It should be stressed that here we consider the estimates from the full-depth data profiles. Figure 9a shows the survey-median values of the turbulent dissipation rates derived using the TSM and the FSP framework. Note that the survey median $\varepsilon_K^{FSP}$ was derived for the depth range between 120 m and 360 m.

In the layer at the depths from 70 m to 180 m, the survey-median values of $\varepsilon_K$ are significantly greater than the survey-median values of $\varepsilon_K^{FSP}$. The survey-median $\varepsilon_K$ ranged from $10^{-8}$ to $10^{-10}$ W kg$^{-1}$, while the survey-median values ranged between $2 \cdot 10^{-10}$ and $10^{-10}$ W kg$^{-1}$. The difference between the survey-median values of $\varepsilon_K$ and $\varepsilon_K^{FSP}$ decreases with increasing depth to 180 m. In the layer at the depths from 180 to 250 m, both estimates have the same order of magnitude, although the survey-median $\varepsilon_K$ varies more widely between $5 \cdot 10^{-11}$ and $1 \cdot 10^{-10}$ W kg$^{-1}$. In the deeper layers from 250 to 320 m, the survey median $\varepsilon_K^{FSP}$ is 3 to 10 times greater than the survey median $\varepsilon_K$, which does not exceed $10^{-10}$ W kg$^{-1}$. Note that at the depths from 320 to 350 m, the survey-averaged $\varepsilon_K$ values increase to $1.5 \cdot 10^{-10}$ W kg$^{-1}$.

Overall, in the upper layer at the depths from 70 to 150 m, the FSP framework underestimates the turbulent dissipation due to the omission of the vertical shortwave disturbance contribution to the shear and strain variances. By contrast, TSM estimations based on high-vertical-resolution measurements can account for this contribution. When the depth increases, the contribution of the vertical shortwave disturbances to the turbulent dissipation rate decreases; thus, the estimates of the survey-median $\varepsilon_K$ become closer to the estimates of the survey-median $\varepsilon_K^{FSP}$. At the depths greater than 250 m, the lower values of the survey-median $\varepsilon_K$ may be caused by underestimation due to weak stratification.

The difference between the survey-median estimates of $\varepsilon_K$ and $\varepsilon_K^{FSP}$ leads to discrepancies between the survey-median values of $K_\rho$ and $K_\rho^{FSP}$ given the nonlinear dependence of $N^2$ on depth. Substantial discrepancies occur in the layer at the depths from 70 to 200 m, where the survey-median estimates of $K_\rho$ obtained by using the TSM exceed by more than one order of magnitude the estimates derived using the FSP framework. In the deep layer at the depths from 270 m to 350 m, the survey median $K_\rho^{FSP}$ is approximately five times greater than the survey median $K_\rho$.

Finally, let us compare the turbulent dissipation rates derived by applying both methods to the data binned into two layers as follows: the upper layer at the depths from 70 to 150 m and the lower layer at the depths from 150 to 250 m (Fig. 10). Notice that here we analyze the daily median values of the dissipation rates.

In the upper layer, the depth-median values of $\varepsilon_K \approx 1.2 \cdot 10^{-9}$ W kg$^{-1}$ usually exceed those of $\varepsilon_K^{FSP} \approx 1.2 \cdot 10^{-10}$ W kg$^{-1}$ by one order of magnitude (Fig. 10a). From early July through mid-October, the depth-median values of $\varepsilon_K$ exceeded the depth-median values of $\varepsilon_K^{FSP}$ by approximately one order of magnitude. By contrast, at the depths of 150 m to 250 m, the median values of $\varepsilon_K$ and $\varepsilon_K^{FSP}$ are often close to each other (Fig. 10b). In this layer, the vertical longwave disturbances dominate the variations of vertical shear and strain. Their spectra are similar to Garrett-Munk spectra (Ostrovskii et al, 2021), and the FSP framework is better suited for estimating the turbulent dissipation rate. Notice that in the lower layer, the TSM may underestimate the turbulent dissipation rate due to weakening of the density stratification, reducing the accuracy of the estimate of the turbulent patch length. The cross-evaluation of both methods is helpful for understanding the uncertainties involved in the estimation of the turbulent dissipation rate.

## 5.2 Depth profile of the diapycnal diffusivity compiled from two sets of estimates based on the TSM and FSP approach

To model realistic mixing in a numerical simulation, the proper parameterization must be specified using resolved scale parameters. Based on the survey-median estimates of $K_\rho$ and $K_\rho^{FSP}$ (Fig. 11), it is desirable to compile a background profile of diapycnal diffusivity accounting for the features of vertical mixing addressed by both TSM and FSP. The upper part of the survey-median $K_\rho$ profile provides a better description of the background profile of the diapycnal diffusivity in the depth range from 70 to approximately 190 m because the TSM correctly accounts for the contribution of shortwave disturbances. In the mid-depth range from 190 to 280 m, the estimated survey-median values of $K_\rho$ and $K_\rho^{FSP}$ obtained by both methods are rather close to each other. Finally, in the lower part from 280 to 350 m depth, the survey-median $K_\rho^{FSP}$ values better represented the background profile of the diapycnal diffusivity. Overall, a strong nonlinear change in diapycnal diffusivity with depth is observed. Below the mixed layer (from 65 to 190 m) where the density stratification is strong, the background diapycnal diffusivity exhibits two maxima. One of these is associated with the lower boundary of the mixed layer, and the other is associated with the layer with maximal values of $V_z$ (see Ostrovskii et al (2021)). Below, a quasi-exponential decrease of the diapycnal diffusivity is observed (from $8 \cdot 10^{-5}$ to $10^{-5}$ m$^2$ s$^{-1}$). At the depths of 180–250 m, a weakly stratified layer is present, where the background diapycnal diffusivity varies from $3 \cdot 10^{-6}$ m$^2$ s$^{-1}$ to $10^{-5}$ m$^2$ s$^{-1}$. This depth range includes the upper boundary of the East Sea Intermediate Water (ESIW) (Yamada et al, 2004; Park et al, 2014; Yoshikawa et al, 1999; Yoon and

Kawamura, 2002; Lee et al, 2011; Park and Lim, 2018). The low values of the background diapycnal diffusivity suggest that only short-term events associated with mesoscale eddies and strong near-inertial waves, as well as double diffusion processes, may be responsible for the intermittently higher diffusivity and vertical exchange between the ESIW and the upper layer (Ostrovskii et al, 2021; Stepanov et al, 2023). In the lower part of the water column, the increase in the background diapycnal diffusivity with depth can be associated with the interaction of shear flow (Primorye Current) with the continental slope. Such interactions can induce enhanced mixing associated with arrested lee waves (Legg and Klymak, 2008; Klymak et al, 2010). In this layer, the background diapycnal diffusivity increases from $8 \cdot 10^{-6}$ $m^2$ $s^{-1}$ to $2 \cdot 10^{-5}$ $m^2$ $s^{-1}$. Notably, enhanced vertical mixing near the bottom was found in various regions of the open ocean, where the diapycnal diffusivity reached a value higher than $10^{-4}$ $m^2$ $s^{-1}$ (Kunze et al, 2002). Diapycnal diffusivity reaches a value of $5 \cdot 10^{-5}$ $m^2$ $s^{-1}$ near the Yermak Plateau (Fer et al, 2010) and reaches approximately $10^{-4}$ $m^2$ $s^{-1}$ in the Storfjorden Fjord (Fer, 2006).

# 6 Conclusions

This study addressed the vertical mixing induced by shear-driven turbulence in the continental slope region of the northwestern Sea. Based on the high-resolution vertical profiles of temperature and salinity obtained by an Aqualog profiler, the spatial scales of the turbulent patches in the density profiles were estimated using the Thorpe-scale method. Based on the relation between the Ozmidov and Thorpe scales and the Osborn relation, the turbulent dissipation rate and the diapycnal diffusivity were obtained in the intermediate layer at the depths from 70 to 260 m. The vertical heat and salt fluxes in this layer were also derived. Quantitative estimates of the turbulent mixing showed that in the depth range from 70 to 150 m, the turbulent dissipation rate and the diapycnal diffusivity reached higher values relative to the underlying water layer at the depth greater than 150 m. Strong turbulent mixing resulted in the intensification of the vertical turbulent exchange of heat and salt. The downward vertical heat flux could exceed 10.0 W $m^{-2}$, and the upward vertical salt flux ranged from $-5 \cdot 10^{-9}$ to $3 \cdot 10^{-9}$ (kg salt) (kg seawater)$^{-1}$ m $s^{-1}$.

We compared the survey-median full-depth profiles of the turbulent dissipation rate derived by using the Thorpe-scale method and the finescale parameterization framework and found that both estimates were of the same order of magnitude only in the layer at the depths from 200 to 280 m. In the upper layer at the depths from about 70 to 150 m, the Thorpe-scale method estimate of the turbulent dissipation rate was significantly (approximately one order of magnitude) greater than that of the finescale parameterization framework. We suppose that this difference is due to the limitations of the finescale parameterization framework, which does not fully account for the contribution of vertical shortwave disturbances to the shear and strain variations. By contrast, for the lower part of the water column at the depth greater than 260 m, we found that the turbulent dissipation rate estimated using the finescale parameterization framework tends to be higher than that derived using the Thorpe-scale method. This discrepancy may be associated with the limitations of the Thorpe scale method under weak density stratification. Smith (2020) modified the Thorpe-scale method by estimating the available overturn potential energy and ignoring the abovementioned discrepancies under weak density stratification. We hope to apply Smith's approach in our future studies. In our opinion,

the Thorpe-scale method yields a robust estimate of the vertical mixing intensity in the subsurface layer, and the finescale parameterization framework is more suitable for application to the deeper layer. This comparison highlights the necessity of choosing appropriate methods and frameworks to obtain reliable quantitative estimates of the vertical mixing intensity from the surface to the bottom of the sea in regions with strong seasonal variations in stratification and multiscale dynamics.

The generalized profile for background diapycnal diffusivity includes the estimates of diapycnal diffusivity obtained using both the Thorpe-scale method and finescale parameterization framework. This model shows strong nonlinear behavior with depth and can be useful for improving the performance of high-resolution ocean general circulation models of basin-wide cyclonic gyre in the northern part of the Sea.

**Acknowledgments** This work was supported by the Russian Science Foundation, grant no. 23-27-00333, https://rscf.ru/project/23-27-00333/.

**Data Availability** The datasets generated during the current study are available https://www.researchgate.net/publication/377629132_mix_Ocean_Dyn.

# 7 Declarations

**Conflict of interest** The authors declare no competing interests.

# References

Amante C, Eakins BW (2009) ETOPO1 1 Arc-Minute Global Relief model: Procedures, Data Sources and Analysis. Report, NOAA Technical Memorandum NESDIS NGDC-24, https://doi.org/10.7289/V5C8276M

Cairns JL, Williams GO (1976) Internal wave observations from a midwater float, 2. J Geophys Res 81(12):1943–1950. https://doi.org/10.1029/JC081i012p01943

Chang KI, Zhang CI, Park C, et al (2015) Oceanography of the East Sea (Japan Sea). Springer, https://doi.org/10.1007/978-3-319-22720-7

Dillon TM (1982) Vertical overturns: A comparison of Thorpe and Ozmidov length scales. J Geophys Res 87(C12). https://doi.org/10.1029/JC087iC12p09601

Dougherty JP (1961) The anisotropy of turbulence at the meteor level. Journal of Atmospheric and Terrestrial Physics 21(2-3):210–213. https://doi.org/10.1016/0021-9169(61)90116-7

Efron B, Gong G (1983) A Leisurely Look at the Bootstrap , the Jackknife , and A Leisurely Look at the Bootstrap , the Jackknife , and. The American Statistician 37(1):36–48

Fer I (2006) Scaling turbulent dissipation in an Arctic fjord. Deep-Sea Res Pt II 53(1-2):77–95. https://doi.org/10.1016/j.dsr2.2006.01.003

Fer I, Skogseth R, Geyer F (2010) Internal waves and mixing in the Marginal Ice Zone near the Yermak Plateau. J Phys Oceanogr 40(7):1613–1630. https://doi.org/10.1175/2010jpo4371.1

Gamo T, Nakayama N, Takahata N, et al (2014) The Sea of Japan and Its Unique Chemistry Revealed by Time-Series Observations over the Last 30 Years. Monographs on Environment, Earth and Planets 2(1):1–22. https://doi.org/10.5047/meep.2014.00201.0001

Garrett C, Munk W (1972) Oceanic mixing by breaking internal waves. Deep-Sea Res Oceanogr Abstr 19(12):823–832. https://doi.org/10.1016/0011-7471(72)90001-0

Gregg MC, Kunze E (1991) Shear and strain in Santa Monica Basin. J Geophys Res 96(C9). https://doi.org/10.1029/91jc01385

Gregg MC, Sanford TB, Winkel DP (2003) Reduced mixing from the breaking of internal waves in equatorial waters. Nature 422(6931):513–515. https://doi.org/10.1038/nature01507

Gregg MC, D'Asaro EA, Riley JJ, et al (2018) Mixing efficiency in the ocean. Ann Rev Mar Sci 10:443–473. https://doi.org/10.1146/annurev-marine-121916-063643

Henyey FS, Wright J, Flatté SM (1986) Energy and action flow through the internal wave field: An eikonal approach. J Geophys Res 91(C7):8487. https://doi.org/10.1029/JC091iC07p08487

Hibiya T, Furuichi N, Robertson R (2012) Assessment of fine-scale parameterizations of turbulent dissipation rates near mixing hotspots in the deep ocean. Geophys Res Lett 39(24). https://doi.org/10.1029/2012gl054068

Inoue R, Yamazaki H, Wolk F, et al (2007) An estimation of Buoyancy Flux for a Mixture of Turbulence and Double Diffusion. J Phys Oceanogr 37(3):611–624. https://doi.org/10.1175/jpo2996.1

Jeon C, Park JH, Varlamov SM, et al (2014) Seasonal variation of semidiurnal internal tides in the East/Japan Sea. J Geophys Res 119(5):2843–2859. https://doi.org/10.1002/2014JC009864

Kawaguchi Y, Wagawa T, Yabe I, et al (2021) Mesoscale-dependent near-inertial internal waves and microscale turbulence in the Tsushima Warm Current. J Oceanogr 77(2):155–171. https://doi.org/10.1007/s10872-020-00583-1

Kim K, Kim KR, Min DH, et al (2001) Warming and structural changes in the east (Japan) Sea: A clue to future changes in global oceans? Geophys Res Lett 28(17):3293–3296. https://doi.org/10.1029/2001GL013078

Kim K, Kim G, Kim K, et al (2002) A sudden bottom-water formation during the severe winter 2000–2001: The case of the East/Japan Sea. Geophys Res Lett 29(8):75–71. https://doi.org/10.1029/2001GL014498

Klymak JM, Legg S, Pinkel R (2010) A Simple Parameterization of Turbulent Tidal Mixing near Supercritical Topography. J Phys Oceanogr 40(9):2059–2074. https://doi.org/10.1175/2010JPO4396.1

Kunze E, Schmitt RW, Toole JM (1995) The Energy Balance in a Warm-Core Ring's Near-Inertial Critical Layer. J Phys Oceanogr 25(5):942–957. https://doi.org/10.1175/1520-0485(1995)025⟨0942:TEBIAW⟩2.0.CO;2

Kunze E, Rosenfeld L, Carter G, et al (2002) Internal waves in Monterey Submarine Canyon. J Phys Oceanogr 32(6):1890–1913. https://doi.org/10.1175/1520-0485(2002)032⟨1890:Iwimsc⟩2.0.Co;2

Kunze E, Firing E, Hummon JM, et al (2006) Global Abyssal Mixing Inferred from Lowered ADCP Shear and CTD Strain Profiles. J Phys Oceanogr 36(8):1553–1576. https://doi.org/10.1175/jpo2926.1

Lazaryuk AY, Kaplunenko DD, Ostrovskii AG, et al (2017) Experimental studies of the thermohaline structure at the continental slope in the northwestern Japan Sea. Journal of Oceanological Research (45):33–51. https://doi.org/10.29006/1564-2291.jor-2017.45(1).5

Lee C, Chang K, Lee JH, et al (2014) Vertical mixing due to double diffusion in the tropical western Pacific. Geophys Res Lett 41(22):7964–7970. https://doi.org/10.1002/2014GL061698

Lee HJ, Park JH, Wimbush M, et al (2011) Tidal Effects on Intermediate Waters: A Case Study in the East/Japan Sea. J Phys Oceanogr 41(1):234–240. https://doi.org/10.1175/2010jpo4510.1

Legg S, Klymak J (2008) Internal Hydraulic Jumps and Overturning Generated by Tidal Flow over a Tall Steep Ridge. J Phys Oceanogr 38(9):1949–1964. https://doi.org/10.1175/2008JPO3777.1

Lim S, C. J. Jang ISO, Park J (2012) Climatology of the mixed layer depth in the East/Japan Sea. J Mar Syst 96-97:1–14. https://doi.org/10.1016/j.jmarsys.2012.01.003

Lique C, Guthrie JD, Steele M, et al (2014) Diffusive vertical heat flux in the Canada Basin of the Arctic Ocean inferred from moored instruments. J Geophys Res 119(1):496–508. https://doi.org/10.1002/2013jc009346

MacKinnon J, Laurent LS, Garabato ACN (2013) Diapycnal Mixing Processes in the Ocean Interior, vol 103, Elsevier BV, pp 159–183. https://doi.org/10.1016/b978-0-12-391851-2.00007-6

MacKinnon JA, Zhao Z, Whalen CB, et al (2017) Climate process team on internal wave-driven ocean mixing. Bull Amer Meteor Soc 98(11):2429–2454. https://doi.org/10.1175/BAMS-D-16-0030.1

Mashayek A, Salehipour H, Bouffard D, et al (2017) Efficiency of turbulent mixing in the abyssal ocean circulation. Geophys Res Lett 44(12):6296–6306. https://doi.org/10.1002/2016GL072452

McDougall T, Barker P (2011) Getting started with TEOS-10 and the Gibbs Seawater (GSW) Oceanographic Toolbox. CSIRO Marine and Atmospheric Research

Meyer A, Sloyan BM, Polzin KL, et al (2015) Mixing variability in the Southern Ocean. J Phys Oceanogr 45(4):966–987. https://doi.org/10.1175/jpo-d-14-0110.1

Miles JW (1961) On the stability of heterogeneous shear flows. J Fluid Mech 10(04):496–508. https://doi.org/10.1017/S0022112061000305

Munk W, Anderson E (1948) Notes on a theory of the thermocline. Journal of Marine Research 7(3):276–295

Nikurashin M, Ferrari R, Grisouard N, et al (2014) The impact of finite-amplitude bottom topography on internal wave generation in the Southern Ocean. J Phys Oceanogr 44(11):2938–2950. https://doi.org/10.1175/JPO-D-13-0201.1

Osborn TR (1980) Estimates of the Local Rate of Vertical Diffusion from Dissipation Measurements. J Phys Oceanogr 10(1):83–89. https://doi.org/10.1175/1520-0485(1980)010⟨0083:eotlro⟩2.0.co;2

Ostrovskii A, Stepanov D, Kaplunenko D, et al (2021) Turbulent mixing and its contribution to the oxygen flux in the northwestern boundary current region of the japan/east sea, april–october 2015. J Mar Syst 224:103619. https://doi.org/10.1016/j.jmarsys.2021.103619

Ostrovskii A, Kubryakov A, Shoev D, et al (2023) Mesoscale Anticyclonic Eddies in the Primorye Current System of the Japan Sea in Summer. Oceanology 63(5):609–622. https://doi.org/10.1134/S0001437023050107

Ozmidov R (1965) Certain features of the energy spectrum of oceanic turbulence. Dokl Akad Nauk SSSR 161(4):828–831

Park J, Lim B (2018) A new perspective on origin of the East Sea Intermediate Water: Observations of Argo floats. Prog Oceanogr 160:213–224. https://doi.org/10.1016/j.pocean.2017.10.015

Park KA, Kang CK, Kim KR, et al (2014) Role of sea ice on satellite-observed chlorophyll-a concentration variations during spring bloom in the East/Japan Sea. Deep-Sea Res Pt I 83:34–44. https://doi.org/10.1016/j.dsr.2013.09.002

Podymov O, Zatsepin A, Kubryakov A, et al (2020) Seasonal and interannual variability of vertical turbulent exchange coefficient in the Black Sea pycnocline in 2013–2016 and its relation to variability of mean kinetic energy of surface currents. Ocean Dyn 70(2):199–211. https://doi.org/10.1007/s10236-019-01331-w

Polzin KL, Toole JM, Schmitt RW (1995) Finescale Parameterizations of Turbulent Dissipation. J Phys Oceanogr 25(3):306–328. https://doi.org/10.1175/1520-0485(1995)025⟨0306:

fpotd⟩2.0.co;2

Polzin KL, Garabato ACN, Huussen TN, et al (2014) Finescale parameterizations of turbulent dissipation. J Geophys Res 119(2):1383–1419. https://doi.org/10.1002/2013jc008979

Radko T, Smith DP (2012) Equilibrium transport in double-diffusive convection. J Fluid Mech 692:5–27. https://doi.org/10.1017/jfm.2011.343

Ruddick B (1983) A practical indicator of the stability of the water column to double-diffusive activity. Deep Sea Research Part A, Oceanographic Research Papers 30(10):1105–1107. https://doi.org/10.1016/0198-0149(83)90063-8

Smith JA (2020) A comparison of two methods using thorpe sorting to estimate mixing. J Atmos Oceanic Technol 37:3–15. https://doi.org/10.1175/JTECH-D-18-0234.1

Stansfield K, Garrett C, Dewey R (2001) Probability distribution of the Thorpe displacement within overturns in Juan de Fuca Strait. J Phys Oceanogr 31(12):3421–3434. https://doi.org/10.1175/1520-0485(2001)031⟨3421:TPDOTT⟩2.0.CO;2

Stepanov DV, Ostrovskii AG, Lazaryuk AY (2023) Diapycnal Mixing and Double Diffusion over the Continental Slope in the Northern Sea of Japan in the Warm Half-Year. Izv Atmos Ocean Phys (Engl Transl) 59(5):572–582. https://doi.org/10.1134/S0001433823050109

Talley LD, Lobanov V, Ponomarev V, et al (2003) Deep convection and brine rejection in the Japan Sea. J Geophys Res 30(4):1159. https://doi.org/10.1029/2002gl016451

Talley LD, Min DH, Lobanov V, et al (2006) Japan/East Sea Water Masses and their relation to the Sea's Circulation. Oceanography 19(3):32–49. https://doi.org/10.5670/oceanog.2006.42

Thompson AF, Gille ST, MacKinnon JA, et al (2007) Spatial and temporal patterns of small-scale mixing in Drake Passage. J Phys Oceanogr 37(3):572–592. https://doi.org/10.1175/JPO3021.1

Thorpe S (1977) Turbulence and mixing in a Scottish Loch. Philos Trans Roy Soc London 286(1334):125–181. https://doi.org/10.1098/rsta.1977.0112

Waterhouse AF, MacKinnon JA, Nash JD, et al (2014) Global Patterns of Diapycnal Mixing from Measurements of the Turbulent Dissipation Rate. J Phys Oceanogr 44(7):1854–1872. https://doi.org/10.1175/jpo-d-13-0104.1

Whalen CB, MacKinnon JA, Talley LD, et al (2015) Estimating the Mean Diapycnal Mixing Using a Finescale Strain Parameterization. J Phys Oceanogr 45(4):1174–1188. https://doi.org/10.1175/jpo-d-14-0167.1

Wijesekera HW, Jarosz E, Wang DW, et al (2022) Tidally Driven Mixing "Hot Spot" at the Entrance of the Japan/East Sea. Geophys Res Lett 49(18):1–10. https://doi.org/10.1029/2022GL100315

Wunsch C, Ferrari R (2004) Vertical mixing, energy, and the general circulation of the oceans. Annu Rev Fluid Mech 36:281–314. https://doi.org/10.1146/annurev.fluid.36.050802.122121

Yamada K, Ishizaka J, Kim SYHC, et al (2004) Seasonal and interannual variability of sea surface chlorophyll a concentration in the Japan/East Sea (JES). Prog Oceanogr 61(2-4):193–211. https://doi.org/10.1016/j.pocean.2004.06.001

Yang Q, Zhao W, Liang X, et al (2017) Elevated mixing in the periphery of mesoscale eddies in the South China Sea. J Phys Oceanogr 47(4):895–907. https://doi.org/10.1175/JPO-D-16-0256.1

Yaroshchuk IO, Leont'ev AP, Kosheleva AV, et al (2016) On intense internal waves in the coastal zone of the Peter the Great Bay (the Sea of Japan). Russ Meteorol Hydro 41(9):629–634. https://doi.org/10.3103/s1068373916090053

Yoon JH, Kawamura H (2002) The formation and circulation of the Intermediate Water in the Japan Sea. J Oceanogr 58(1):197–211. https://doi.org/10.1023/A:1015893104998

Yoshikawa Y, Awaji T, Akitomo K (1999) Formation and circulation processes of intermediate water in the Japan Sea. J Phys Oceanogr 29(8):1701–1722. https://doi.org/10.1175/1520-0485(1999)029⟨1701:Facpoi⟩2.0.Co;2

You J, Xu Z, Li Q, et al (2021) Enhanced internal tidal mixing in the Philippine Sea mesoscale environment. Nonlinear Process Geophys 28(2):271–284. https://doi.org/10.5194/npg-28-271-2021

Zoubir A, Boashash B (1998) The bootstrap and its application in signal processing. IEEE Signal Processing Magazine 15(1):56–76. https://doi.org/10.1109/79.647043

## FIGURE CAPTIONS

**Fig. 1** Survey-averaged geostrophic circulation data were obtained from the AVISO dataset (https://www.aviso.altimetry.fr/en/data/data-access.html), and the colored topography was obtained from the ETOPO1 (Amante and Eakins, 2009) in the northwestern Sea. The location of the Aqualog profiler mooring station is shown by the red asterisk.

**Fig. 2** An example of a density profile ($\sigma_\theta$) at 00 h 18 s on 26 April 2015 and the corresponding profiles of (b) buoyancy frequency ($N$) of the turbulent patches, (c) Thorpe displacement ($L_D = (z_n - z_m)$) (3), (d) Thorpe scale ($L_T$), and (e) dissipation rates ($\varepsilon_K$) obtained using Thorpe scale analysis.

**Fig. 3** The time-depth plot of the background buoyancy frequency ($N$) estimated from all profiles. Values of $N < 10^{-1}$ cph were excluded from the analysis.

**Fig. 4** Time-depth plot of the gradient Richardson number ($Ri$) estimated from all data. The white dots indicate the regions of the data profiles that experienced favorable conditions for double diffusion.

**Fig. 5** Time-depth plot of the turbulent dissipation rate ($\varepsilon_K$,W kg$^{-1}$) (a) and diapycnal diffusivity ($K_\rho$, m$^2$ s$^{-1}$) (b) derived using the Thorpe-scale method and full-depth data profiles. The values of $\varepsilon_K > 10^{-8}$ W kg$^{-1}$ and $K_\rho > 10^{-4}$ m$^2$ s$^{-1}$ are shown by large markers. The values of $\varepsilon_K < 10^{-20}$ W kg$^{-1}$ and $K_\rho < 10^{-7}$ m$^2$ s$^{-1}$ are not shown. Notice that the upper parts of the profiles are plotted to show the data in more detail.

**Fig. 6** The survey-median values of the turbulent dissipation rate ($\varepsilon_K$, W kg$^{-1}$) (a) and the diapycnal diffusivity ($K_\rho$, m$^2$ s$^{-1}$) (b) derived by applying the Thorpe-scale method for processing the full-depth profiles of $\sigma_\theta$. The 95% bootstrap confidence intervals are shown with color shading.

**Fig. 7** The survey median values of the turbulent dissipation rate ($\varepsilon_K$, W kg$^{-1}$) (a) and the diapycnal diffusivity ($K_\rho$, m$^2$ s$^{-1}$) (b) derived by applying the Thorpe-scale method to all of the data profiles. The 95% bootstrap confidence intervals are shown with color shading.

**Fig. 8** Time-depth plot of the vertical heat flux ($Q$, W m$^{-2}$ (a)) and salt flux ($J_S$, (kg salt) (kg seawater)$^{-1}$ m s$^{-1}$) (b) estimated following formula (5) from all of the data. The positive values are for the downward-directed fluxes.

**Fig. 9** The survey-median turbulent dissipation rate (a) and the diapycnal diffusivity profiles (b) derived using the Thorpe-scale method (TSM, red lines) and the finescale parameterization framework (FSP, blue lines) from the full-depth data profiles. The 95% bootstrapped confidence intervals are shown with corresponding color shading.

**Fig. 10** Daily mean time series of the depth-median values of the turbulent dissipation rate derived using the Thorpe-scale method (TSM, red lines) and the finescale parameterization framework (FSP, blue lines) from all of the data binned into two layers: (a) at the depths of 70-150 m and (b) at the depths of 150-250 m.

**Fig. 11** Background diapycnal diffusivity data composed of survey median values of diapycnal diffusivity $K_\rho$ and $K_\rho^{FSP}$ derived via the Thorpe-scale method (TSM, red bars) and the finescale parameterization framework (FSP, blue bars), respectively.

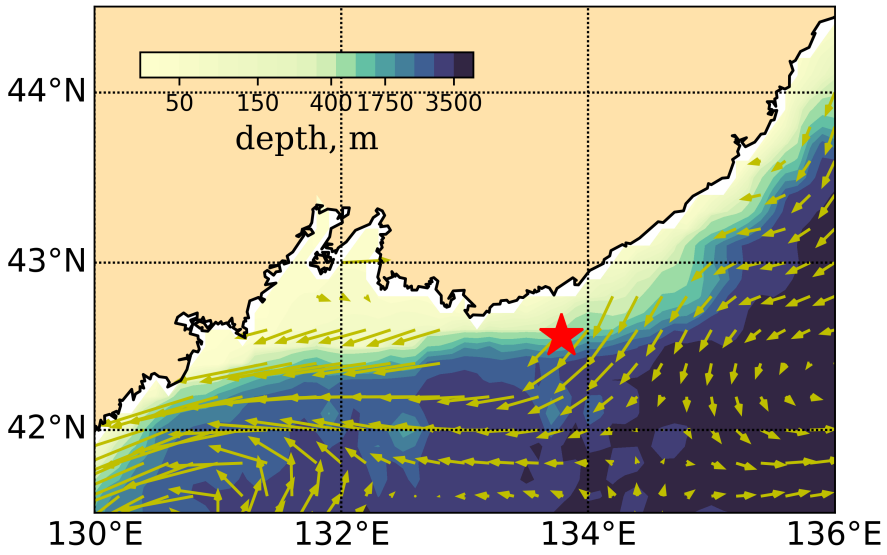


**Fig. 1** Survey-averaged geostrophic circulation data were obtained from the AVISO dataset (https://www.aviso.altimetry.fr/en/data/data-access.html), and the colored topography was obtained from the ETOPO1 (Amante and Eakins, 2009) in the northwestern Sea. The location of the Aqualog profiler mooring station is shown by the red asterisk.

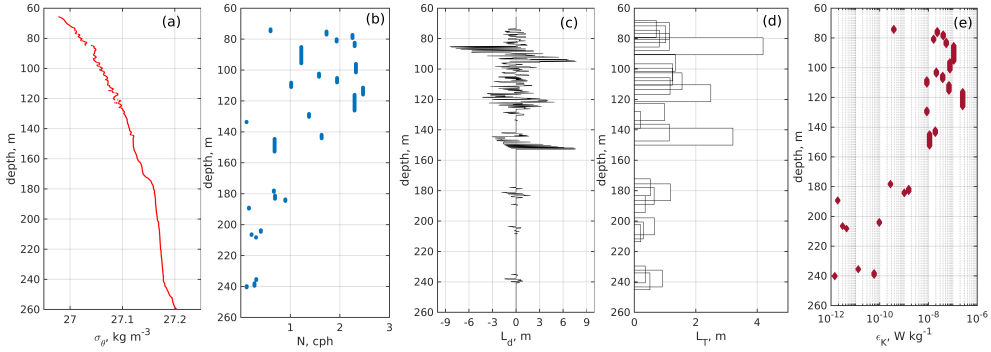


**Fig. 2** An example of a density profile ($\sigma_\theta$) at 00 h 18 s on 26 April 2015 and the corresponding profiles of (b) buoyancy frequency ($N$) of the turbulent patches, (c) Thorpe displacement ($L_D = (z_n - z_m)$) (3), (d) Thorpe scale ($L_T$), and (e) dissipation rates ($\varepsilon_K$) obtained using Thorpe scale analysis.

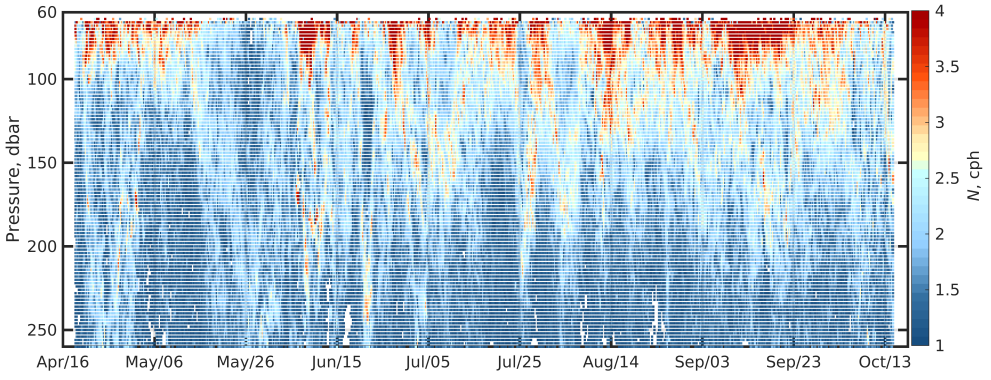


**Fig. 3** The time-depth plot of the background buoyancy frequency ($N$) estimated from all profiles. Values of $N < 10^{-1}$ cph were excluded from the analysis.

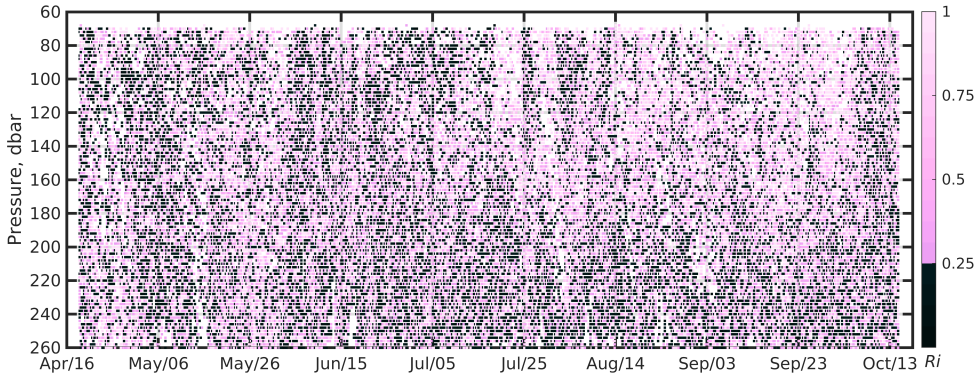


**Fig. 4** Time-depth plot of the gradient Richardson number ($Ri$) estimated from all data. The white dots indicate the regions of the data profiles that experienced favorable conditions for double diffusion.

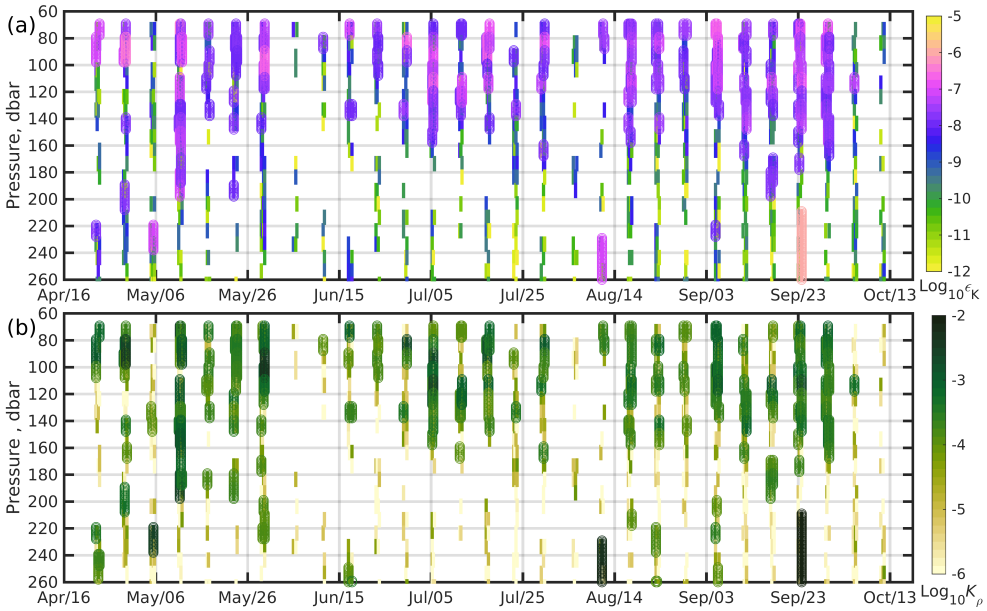


**Fig. 5** Time-depth plot of the turbulent dissipation rate ($\varepsilon_K$,W kg$^{-1}$) (a) and diapycnal diffusivity ($K_\rho$, m$^2$ s$^{-1}$) (b) derived using the Thorpe-scale method and full-depth data profiles. The values of $\varepsilon_K > 10^{-8}$ W kg$^{-1}$ and $K_\rho > 10^{-4}$ m$^2$ s$^{-1}$ are shown by large markers. The values of $\varepsilon_K < 10^{-20}$ W kg$^{-1}$ and $K_\rho < 10^{-7}$ m$^2$ s$^{-1}$ are not shown. Notice that the upper parts of the profiles are plotted to show the data in more detail.

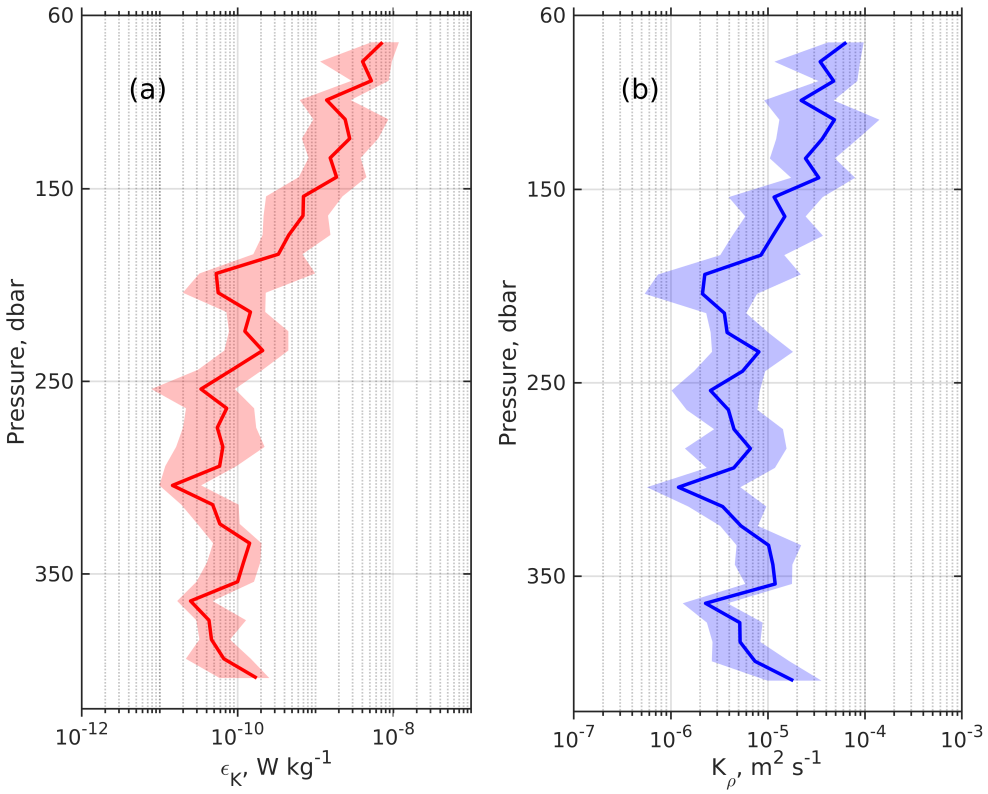


**Fig. 6** The survey-median values of the turbulent dissipation rate ($\varepsilon_K$, W kg$^{-1}$) (a) and the diapycnal diffusivity ($K_\rho$, m$^2$ s$^{-1}$) (b) derived by applying the Thorpe-scale method for processing the full-depth profiles of $\sigma_\theta$. The 95% bootstrap confidence intervals are shown with color shading.

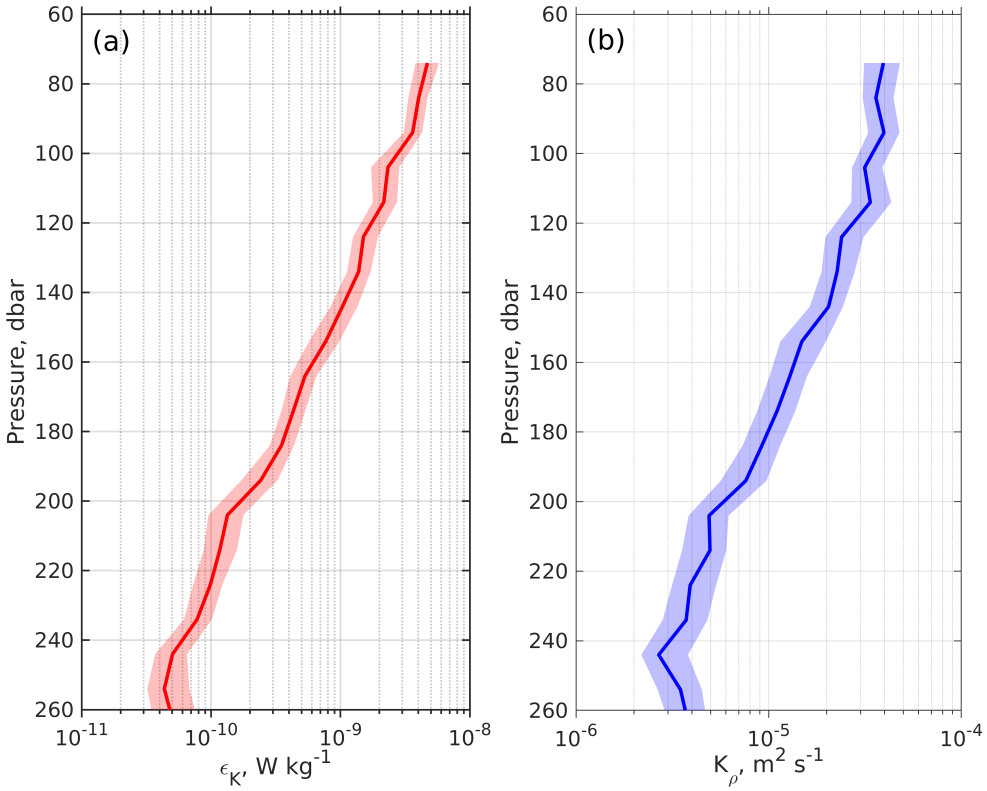


**Fig. 7** The survey median values of the turbulent dissipation rate ($\varepsilon_K$, W kg$^{-1}$) (a) and the diapycnal diffusivity ($K_\rho$, m$^2$ s$^{-1}$) (b) derived by applying the Thorpe-scale method to all of the data profiles. The 95% bootstrap confidence intervals are shown with color shading.

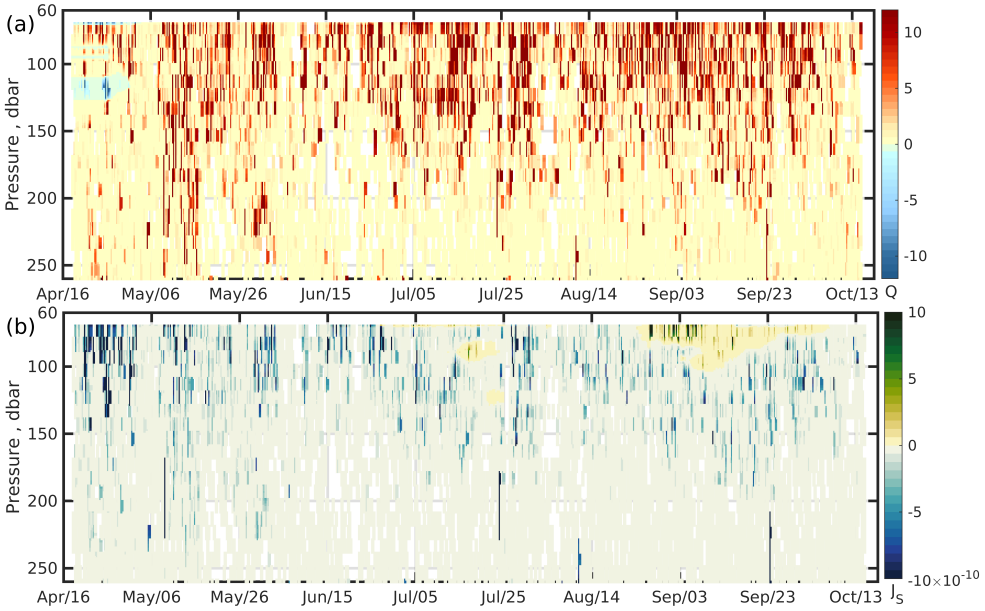


**Fig. 8** Time-depth plot of the vertical heat flux ($Q$, W m$^{-2}$ (a)) and salt flux ($J_S$, (kg salt) (kg seawater)$^{-1}$ m s$^{-1}$) (b) estimated following formula (5) from all of the data. The positive values are for the downward-directed fluxes.

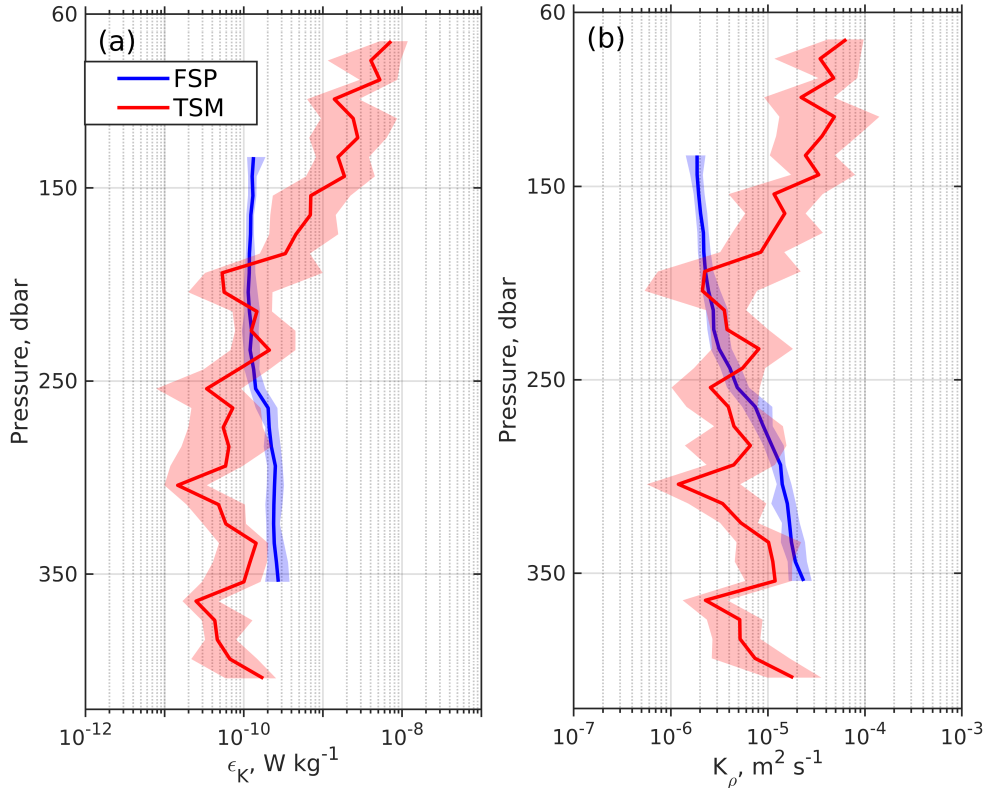


**Fig. 9** The survey-median turbulent dissipation rate (a) and the diapycnal diffusivity profiles (b) derived using the Thorpe-scale method (TSM, red lines) and the finescale parameterization framework (FSP, blue lines) from the full-depth data profiles. The 95% bootstrapped confidence intervals are shown with corresponding color shading.

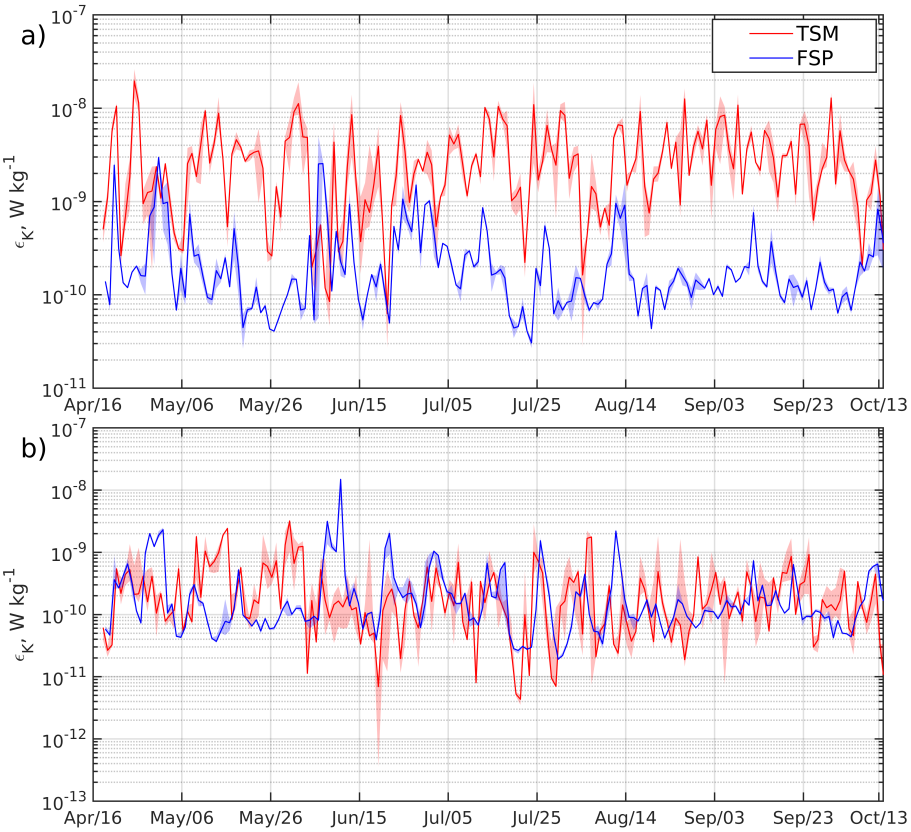


**Fig. 10** Daily mean time series of the depth-median values of the turbulent dissipation rate derived using the Thorpe-scale method (TSM, red lines) and the finescale parameterization framework (FSP, blue lines) from all of the data binned into two layers: (a) at the depths of 70-150 m and (b) at the depths of 150-250 m.

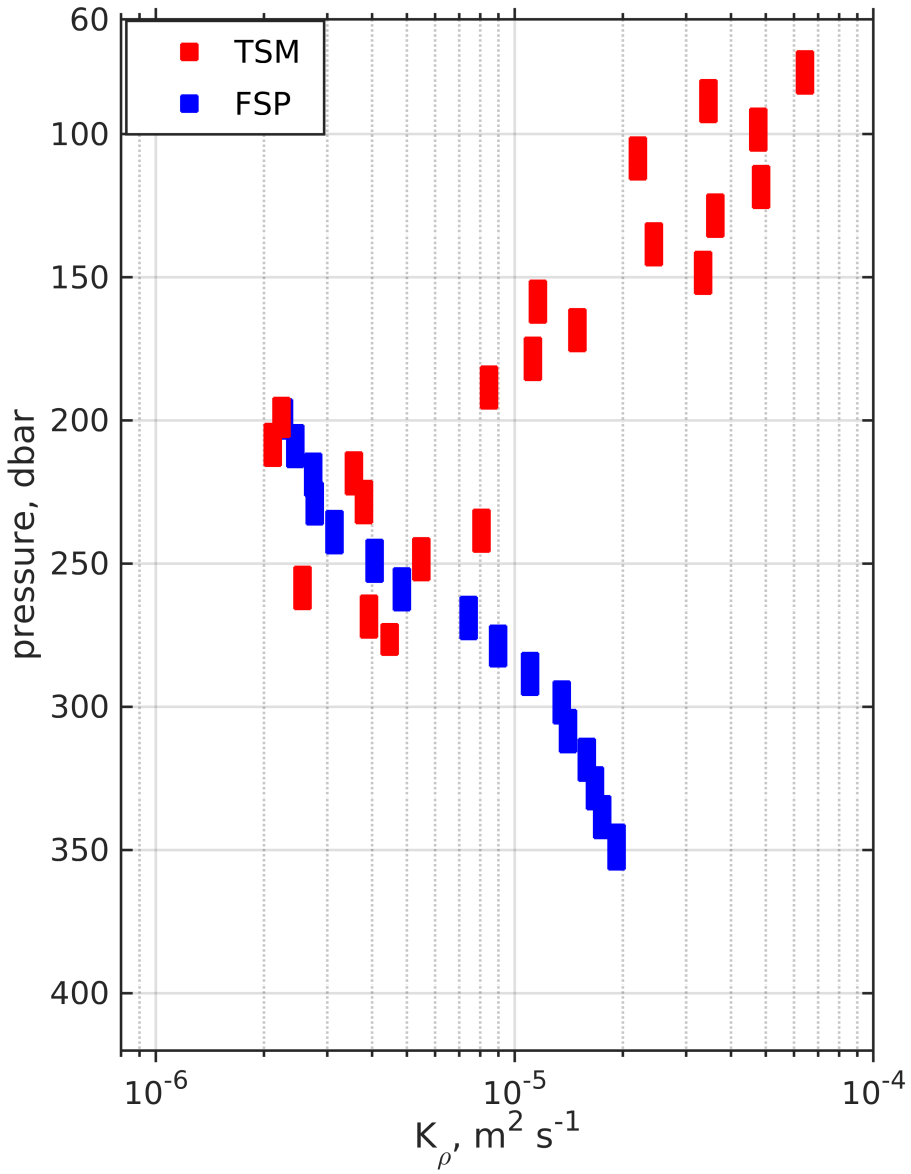


**Fig. 11** Background diapycnal diffusivity data composed of survey median values of diapycnal diffusivity $K_\rho$ and $K_\rho^{FSP}$ derived via the Thorpe-scale method (TSM, red bars) and the finescale parameterization framework (FSP, blue bars), respectively.